Improved O₂-assisted styrene synthesis by double-function purification of SWCNT catalyst

Juan J. Mercadal [a], Alvaro Mayoral [b, c], José Luis G. Fierro [d], Enrique García-Bordejé [e], Ignacio Melián-Cabrera [a, f, *]

[a] Faculty of Science and Engineering, University of Groningen, Nijenborgh 4, 9747 AG Groningen, the Netherlands

[b] Instituto de Nanociencia y Materiales de Aragón (INMA), CSIC-Universidad de Zaragoza, Zaragoza 50009, Spain

[c] Laboratorio de Microscopías Avanzadas (LMA), Universidad de Zaragoza, C/Mariano Esquillor, Edificio I+D, 50018 Zaragoza, Spain

[d] Sustainable Energy and Chemistry Group, Instituto de Catálisis y Petroleoquímica, CSIC, 28049 Madrid, Spain

[e] Instituto de Carboquímica, ICB-CSIC, Miguel Luesma Castán 4, 50018 Zaragoza, Spain

[f] Applied Photochemistry and Materials for Energy Group, University of La Laguna, Avda. Astrofísico Francisco Sánchez, s/n, PO Box 456, 38200 San Cristóbal de La Laguna, S/C de Tenerife, Spain

A B S T R A C T

The catalytic performance of SWCNT was notably improved in the oxidative dehydrogenation of ethylbenzene (EB) to styrene (ST) upon a double-function purification in one step of the raw SWCNT. This consists of lowering the MeO_x concentration and generating surface $C{=}O$ groups after processing it in nitric acid at controlled conditions, while preserving the structure. The textural improvement was ascribed to the cutting of the tubes/bundles by oxidation and to MeO_x removal itself (dilution effect). Both EB conversion and ST selectivity increased with a parallel lowering of the undesired CO_x selectivity. The conversion was interpreted by the enhancement of the intrinsic properties (i.e., more surface ketonic groups) but also to the higher load of SWCNT in the bed upon purification; both factors contribute to a higher number of active sites ($C{=}O$) in the bed for styrene formation. The most purified catalyst underperformed in conversion once the purification altered the SWCNT structure notably. Thus, preserving the structure is an important condition to achieve high conversion and yield. The better selectivity was explained in two ways; more styrene-forming sites ($C{=}O$) or less CO_x-forming sites (uncoated MeO_x) in the bed, or both. The styrene yield per catalyst volume was improved by an average of ca. 240 % in comparison to the non-purified SWCNT. Deactivation is critical in maximizing the purification effect on the intrinsic and volumetric yields. In practical terms, the method proved to enhance the reaction; the selectivity towards the unwanted CO_x was significantly lowered with a gain towards styrene, achieving comparable values as in the conventional process, but operated at much lower temperature.

1. Introduction

Carbon-based materials as heterogeneous catalysts are attractive. In this way, implemented technologies would rely less on critical materials and would become more sustainable [1,2]. A relevant family of materials refers to porous nanostructured carbons. In addition to the extraordinary control in porosity and structure, they can be functionalised with active surface groups, which make them attractive for catalysis [3–7]. Carbon-based heterogeneous catalysis (i.e., metal free) is therefore very attractive, being a sustainable and environmentally benign technology. However, it does pose some challenges. First, the capability to prepare carbon-based catalysts with specific surface functionalities with precision is often limited; normally various types of surface groups are introduced during the preparation steps. Those groups are sometimes unstable towards regeneration, so they need to be reintroduced. Furthermore, transition metal impurities often coexist and their effect,

sometimes adverse, cannot be easily discriminated from the carbon [8]. Purification of the carbon brings some additional challenges; the more it is purified, the more it is modified. Hence, a compromise approach should be taken sometimes.

One reaction that attracts interest refers to the oxidative dehydrogenation of ethylbenzene (EB-ODH) into styrene, where an organocatalysis mechanism takes place. The proposed active site cycle is based on a quinone-to-hydroquinone redox mechanism, where the quinone abstract hydrogens from ethylbenzene (EB) to form styrene (ST), whereas O_2 oxidizes the hydroquinone back into quinone [9,10] (later on in the text we refer it as ketones since this topic is still under debate). This motivated studying many types of carbon-based materials for this reaction, as long as ketonic groups are present in the starting material or introduced by controlled oxidative post-synthesis methods [11–23]. The EB-ODH reaction is considered to be a more efficient route to produce styrene than the direct dehydrogenation; it does not

have equilibrium limitations, and lower temperatures are required. Other process benefits have been claimed elsewhere [24]. Major handicaps for the catalyst are stability issues, the production of undesired CO/CO_2 (denoted as CO_x) as side products and over-coking leading to a severe drop of the textural features. In this case, coke does not act as a poison but brings additional active sites, but too much coke depletes the surface area and leads to a performance decay. Stability is mainly related to coking but there is another aspect, the stability after reactivation. CO_x formation worsens the process economics since such a gas stream has no value; it is a loss of ethylbenzene [2]. Therefore, improvements on coke control, stability and selectivity at practical reaction conditions have been topics of interest [23,25–30].

Some of the successful catalysts for this reaction are carbon nanotubes [21–23]. Their syntheses often require a metal-based catalyst as nucleation point. SWCNTs are produced only via transition metal-based catalysis which means they always contain metallic impurities as by-product after the manufacturing process. Metal impurities can be removed by post-synthesis liquid-phase oxidation with acids [31,32]. However, there is evidence that some metal residue is generally left in the carbon nanotube because such residues are encased by chemically-stable polyhedral graphitic coatings [33]. In some instances, controlled gas-phase oxidation followed by acid treatment can remove most of the metal residue [34,35]. Only high-temperature annealing has proven to produce metal-free carbon nanotubes [32,36], requiring the evaporation/sublimation of the metals at very high temperatures. A 99.9 wt% purity was achieved at 1800 °C for a MWCNT [36]. In the case of SWCNT, this treatment is less effective; a 98 wt% purity was achieved by thermal annealing at 1800 °C and did not improve at 2000 °C [37].

Proven the complexity to fully remove the metal residue (MeO_x) from the carbon nanotubes, it is crucial to understand the effect of such residue on the targeted application. To the best of our knowledge, the impact of the metal residues left in carbon nanotubes for the EB-ODH reaction has not been studied. Kiciński and Dyjak [8] reviewed the role of such metal residues on many applications, though this reaction was not accounted; probably because of the lack of prior studies. The motivation of this work is to understand the MeO_x's role before going into considering an ultra-pure catalyst for this reaction. The motivation also comes from the fact that, in some studies, the metal residue was able to catalyze the oxidation of the nanotube itself during the thermal cleaning [34,35]. As this reaction employs O_2 at ca. 350–475 °C [11–23, 25–30], it may be possible that the metal residue can influence the reaction performance by promoting the CO_x routes.

This reaction has been widely studied by developing new materials as catalysts. However, the typically-studied reaction conditions are far from implementation. One can find too diluted feedstocks and high levels of O_2 (see Table S1 indicating conditions for some literature examples). This brings up two issues. Firstly, the EB concentration should be higher to enhance the volumetric efficiency of the reactor. In other words, a high dilution leads to large reactor volume and energy losses due to diluent heating. Secondly, by operating at high O_2/EB ratios unconverted O_2 downstream the reactor would enter into the distillation section causing explosive conditions. Thus, the reaction should be operated in such a way that O_2 is fully converted to avoid such a situation. This can be solved by using a lower O_2/EB. In this study, practical reaction conditions have been employed; i.e., [EB] of 10 vol% and O_2/EB = 0.6 mol ratio.

This work investigates the purification of a raw MeO_x-containing SWCNT as catalyst for the reaction, where MeO_x is a metal-based residue coming from its manufacturing process. The purification has a double function, lowering the MeO_x content and oxidizing the surface to generate (or add more if those were available) active sites (ketonic groups). The study first characterizes the starting material, then discusses the purification and properties of the purified materials. Finally, the reaction performance at practical conditions is discussed in relation

to the catalyst properties. It is shown that a well-defined purification proved to be very positive for the reaction.

2. Experimental methods

2.1. Materials

The single-walled carbon nanotube (SWCNT) material was supplied by Carbon Solutions Inc. (product code: AP-SWNT), synthesized by the arc discharge method using a Ni/Y catalyst. Note that this material is a not a single SWCNT species but a SWCNT-rich material containing other carbon allotropes. For simplicity, we will denote it as SWCNT. This is further discussed in section 3.1. HNO_3 (ACS reagent, 70 % Sigma Aldrich) was used without further purification. Anhydrous ethylbenzene was purchased from Sigma-Aldrich (99.8 %), and all the compounds used for calibrating the gas chromatograph. The employed gases in the reactor and characterization techniques were of analytical 5.0 grade, i.e., 99.999 % purity. Milli-Q water (Millipore, 18.2 MΩ.cm at 25 °C) was used in the SWCNT cleaning procedure.

2.2. SWCNT purification procedure

The purification of the raw SWCNT was carried out by reflux in a 3 M HNO_3 solution (100 mg of SWCNTs in 10 ml solution). The reflux was achieved using an oil bath equipped with magnetic stirring. A reflux condenser was employed to avoid evaporation of the liquid phase. After the treatment, the slurry was rapidly cooled down to room temperature, diluted with Milli-Q water and filtered through a nanocellulose vacuum filter. The retained solid was washed thoroughly with Milli-Q water to rinse residual acid until achieving neutral washing water. The solid was subsequently dried at 110 °C overnight in a drying oven. The degree of metal removal was controlled by the treatment time. The following times were required for the studied materials: SW (36) is the as-received SWCNT containing ca. 36 wt% MeO_x; SW(17) containing 17 wt% MeO_x required ca. 0.6 h; SW(8) containing 8 wt% MeO_x took ca. 2.5 h and SW(4) containing 4 wt% MeO_x required 24 h treatment. The latter material was formed by very small aggregates that required washing by ultracentrifugation.

2.3. Characterization methods

The total carbon and metal residue contents were quantified by thermogravimetric analysis (TGA). The analysis was carried out on a SDTA851e Mettler-Toledo apparatus where the sample weight was monitored as a function of temperature, from 30 to 900 °C with a heating rate of 3 °C/min using a 100 ml/min STP flow of synthetic air. The proportion of total carbon was quantified by the weight loss between 150 and 900 °C. The final residue in the TGA pattern at 900 °C corresponds to the MeO_x content. The DTGA analysis corresponds to the derivative of the TGA pattern.

The textural features were obtained from the nitrogen physisorption analyses at −196 °C on a Micromeritics ASAP 2020. The materials were treated at 200 °C for 4 h under vacuum prior to the analyses. The surface area was calculated with the BET method (S_{BET}, and termed as BET area) following the recommendations by Thommes et al. for micropores-containing materials [38]. The total pore volume (V_T) was calculated using the single point at the relative pressure 0.98 in the desorption branch [39]. The pore size distributions were obtained using the BJH model in the desorption branch. The micropore and external parameters (V_{micro}, V_{ext} and S_{ext}) were derived from the *t*-plot method. We denoted it as external surface or volume (S_{ext}, V_{ext}) since the materials contribute with pores above 50 nm, thus pores beyond micropores including *meso*- and macropores. Nitrogen in gas adsorption analysis can have limitations when assessing micropores-containing materials.

Therefore, care was given in choosing an appropriate equilibration time.

The XPS measurements were performed on a VG Escalab 200 R spectrometer using a monochromatic Al Kα X-ray source [40,41]. The measurements were performed at ambient temperature and the chamber pressure was about 10^{-7} mbar during the analysis. All spectra were calibrated by setting the binding energy of the main peak in the C1s line at the reference value of ca. 284.4 eV. Deconvolution of O1s spectra was performed using a mixed Gauss-Lorentz function, with a 30 % Lorentzian contribution. The quantification was done using empirical relative sensitivity factors [42].

Raman spectra were obtained with a 785 nm excitation line (30mW) on a Perkin Elmer Raman station 400 spectrometer.

Transmission electron microscopy (TEM) was carried out on a FEI FEG Titan High-base operated at 80 kV to minimize the electron beam damage. The microscope was equipped with a field emission gun (Schottky-FEG) and a spherical aberration corrector (Cs-corrector) for the image formation system. It is also fitted with a CCD Gatan camera $2\,k \times 2\,k$ and a Gatan Tridiem 863 energy filter. The sample was suspended in ethanol and then deposited onto a holey carbon grid until dryness before analysis.

2.4. A note on the XPS interpretation

The O 1 s spectra were used to quantify the oxygenated groups. C 1 s spectra were not used as they are generally more ambiguous as the contributions of the O-containing groups are very low as compared to the whole signal. Each O 1 s spectrum was deconvoluted into four components, corresponding to C=O (ketonic carbonyl groups, ca. 531.3 eV), O=C-O (sum of carboxylic acid, anhydride, lactone, and ester groups, ca. 532.5 eV), C-OH (phenol groups, ca. 533.8 eV) and water (ca. 535.5 eV) [43]. The justification of the O=C-O and its binding energy in [43], in our view, can be understood as an average value between the O*-(C=O)-C and O-(C=O*)-C, from the reported values in [44]. The deconvolution into such species in [43] was later justified with additional experimental evidence; a linear dependency between the XPS C=O and Boehm titration data and XPS C-OH with TPD [45]. Hence, this XPS deconvolution has supporting experimental evidence.

In our XPS-derived calculations, we have indicated them as approximate (∼) since some assumptions were made. First, there can be some accuracy issues with the XPS-derived data in relation to material and instrument. Secondly, the estimation of the μmol/bed requires knowing the fraction of mass where the species are located. We have considered a homogeneous distribution of the species in the whole carbon-based fraction, and the metal-based fraction was excluded. The latter is consistent with the fact that the XPS survey spectra showed mostly C and O (low metals on surface). The homogeneous approach was employed in Wen et al. [45] where good correlations between XPS and other techniques were found. In summary, the XPS-derived data may have accuracy issues. At this stage, they can be considered as a preliminary approximation.

2.5. Catalytic activity measurements

The catalytic tests were performed on an EFFI® micro activity setup. The reaction conditions were industrially relevant, meaning a high EB concentration (ca. 10 vol%), and limited O_2 (O_2/EB = 0.6). The measurements were carried out at constant catalyst bed volume (0.8 ml catalyst) following the procedure already described elsewhere [23,25–30]. The corresponding catalyst weight loads for each material are given in Table S2. The catalyst weights change due to the density changes upon treatment; the materials become denser. The catalyst particle size was 212–425 μm. The reactor feed consisted of a mixture of nitrogen, synthetic air, and ethylbenzene vapor. To create such a feed stream, a liquid ethylbenzene flow of 1 g/h was evaporated (3.54 ml/

min vapor at STP) and mixed with a stream of N_2 and air. The total flowrate was 36 ml/min (STP) with ca. 10 vol% of gas-phase ethylbenzene concentration. The runs were carried out for ca. 9 h with O_2/EB = 0.6 and a temperature of 350 °C. The gas hourly space velocity (GHSV) was 2700 l/l/h. The pressure in the reactor varied in the range of 1.8–2.2 bar. The reactor outlet flow stream was analyzed using an online two-channel gas chromatograph with TCD and FID detectors and a combination of columns (0.3 m Hayesep Q 80–100 mesh with back-flush; 25 m × 0.53 mm Porabond Q, 15 m × 0.53 mm molsieve 5 Å and RTX-1 with 30 m × 0.53 mm). The main reaction products are styrene, CO and CO_2; traces of benzene were observed (1 % selectivity). Before the reaction, the catalyst was heated in a N_2 gas stream up to the reaction temperature and subsequently switched to the reaction mixture, which determined the start of the reaction. The conversion, selectivity and yields were calculated as:

$$X_{EB}\,(\%) = \frac{[\dot{n}_{EB}]_{IN} - [\dot{n}_{EB}]_{OUT}}{[\dot{n}_{EB}]_{IN}} \times 100 \tag{1}$$

$$S_{\mathrm{Pr}\,oduct\,P}\,(\%) = \frac{\dot{n}_{\mathrm{Pr}\,oduct\,P}}{[\dot{n}_{EB}]_{IN} - [\dot{n}_{EB}]_{OUT}} \times 100 \tag{2}$$

$$Y_{\mathrm{Pr}\,oduct\,P}\,(\%) = X_{EB} \cdot S_{\mathrm{Pr}\,oduct\,P}/100 \tag{3}$$

$$\dot{n}_{ST}^{Vol}\,(mol\,ST \cdot h^{-1} \cdot cm_{cat}^{-3}) = \frac{[\dot{n}_{EB}]_{IN} \cdot X_{EB} \cdot S_{ST} \cdot 10^{-4}}{V_{cat}} \tag{4}$$

$$\dot{n}_{ST}^{Carbon}\,(mol\,ST \cdot h^{-1} \cdot g_{Carbon}^{-1})$$
$$= \frac{[\dot{n}_{EB}]_{IN} \cdot X_{EB} \cdot S_{ST} \cdot 10^{-4}}{W_{Carbon}} \tag{5}$$

Where $\dot{n}$-values are the molar flowrates, V_{cat} is the catalyst bed volume and W_{Carbon} is the weight of carbon in bed. In the equations, the terms 'EB' and 'ST' refers to ethylbenzene and styrene.

2.6. A note on the structure and activity correlation

The initial catalyst performance data were employed where a correlation between the activity and characterisation was made. This is because the characterisation of the catalysts was made on the fresh materials. This reaction is known to produce ODH-coke that can modify the catalyst surface (i.e., new surface functional groups and texture). The characterisation of the after-reaction catalysts was not within the scope of this study.

3. Results and discussion

3.1. Nature of the raw carbon nanotube

The single-walled carbon nanotube (SWCNT) was synthesized by arc discharge. Despite the commercial specification classifies it as single-walled carbon nanotube, the fact is that it contains other carbon allotropes. Hence, it is not a single species material. Fig. 1 shows the DTGA pattern highlighting two regions, ascribed to amorphous carbon (lower temperature) and a broad higher-temperature peak [31]. The broad high-temperature peak suggests that besides SWCNT, other types coexist, such as DWCNT or even MWCNT as contaminants. The heterogeneous nature of carbon nanotubes obtained by arch discharge was discussed by Moore et al. [46] who pointed out the difficulty in producing pure SWCNT or DWCNT. Moreover, SWCNT and DWCNT exhibit similar Raman features, and cannot be distinguished. The presence of DWCNT (or MWCNT) impurities can be evaluated by TEM. Based on the TEM data (discussed later), besides amorphous and graphitic domains, the main nanotubes are SWCNT. Accordingly, the material has been denoted as SWCNT. However, the heterogeneity of this commercial material should be kept in mind along the discussion, so it is not a single species but a SWCNT-rich material. As the tubes are generally agglomerated, we will refer it as bundle or tube/bundle. Note that the ac-
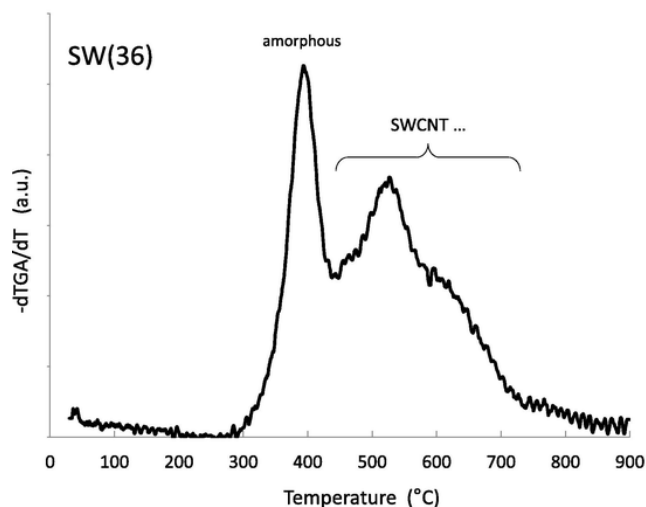
Fig. 1. DTGA analysis of the as-received SWCNT, SW(36).

tive sites (C=O/C-OH) can be located in the SWCNT, in the DWCNT impurities, but also in the amorphous domains; at present we cannot distinguish where these sites are located.

3.2. Demetallization

The thermal analysis of the raw SWCNT revealed a MeO_x content of ca. 36 wt% (Fig. 2). The material will be denoted as SW(36) from now onwards, as well as the purified counterparts as SW(X), where X is the MeO_x residue (wt.%). This material was refluxed in a 3 M HNO_3 solution for ca. 0.6, 2.5 and 24 h following the procedure described by Hu et al. [31], but considering shorter processing times, as a means to adjust the MeO_x content. This resulted in three materials with a MeO_x content of 17, 8 and 4 wt% (Fig. 2, inset). Due to the MeO_x removal, the total carbon content increased from 62 up to 78, 83 and 92 wt%, respectively (Fig. 2, inset). The differences to 100 % correspond to the weight loss from 30 to 150 °C, attributed to physisorbed water, though other

unstable species such as carboxylic groups can count for this as well [47].

It is worth noting that for SW(4) the MeO_x removal was not significant despite it was treated for 24 h (4 wt%) as compared to 2.5 h (8 wt%). Therefore, there are some constraints to lower the MeO_x content. This can be ascribed to the intrinsic nature of the MeO_x (not dissolving easily in HNO_3) or to the encapsulating graphitic carbon that is stable against oxidation, or both effects. About the first concept, there is no comparative study in the literature among various mineral acids for the leaching of Yttrium-based materials (in general, not specifically in SWCNT); H_2SO_4 is often reported as an effective leaching acid [48]. But in this case, sulfonation will compete with oxidation, a situation that is not desirable in order to maximize the C=O/C-OH concentration. About the encapsulation of metal residues within carbon in SWCNTs, Chen et al. [49] found out that Co clusters covered by thick layers of carbon, either amorphous or graphite, cannot be removed by HCl treatment alone. This is likely happening here for the metal residue that is covered by graphitic carbon, as seen by TEM in Fig. 3.

The percentage of surface carbon and metals determined by XPS in the purified SWCNT (Table S3) contrasts with the percentages calculated from TGA (inset Fig. 2, and Table 1). The difference is related to the fact that the MeO_x are largely encapsulated by carbon (graphitic or amorphous), rendering low surface XPS concentrations. This can be seen from the TEM data (Fig. 3 and Figure S1) where MeO_x are covered by graphitic or amorphous carbon. Hence, despite the samples contain large MeO_x loadings (4–36 wt%), MeO_x is occluded within the carbon and not accessible by XPS.

3.3. Purification effects on carbon structure and texture

Cs-corrected TEM data of the starting material revealed various types of carbon allotropes such as bundled SWCNT, DWCNT, graphitic shells enclosing MeO_x particles, amorphous carbon domains (or defective graphite) and isolated SWCNT (Fig. 3). Due to that heterogeneity, the TGA weight loss between 150 and 900 °C was denoted as total carbon (Fig. 2). Figure S1 displays additional TEM data highlighting the amorphous domains in more detail.
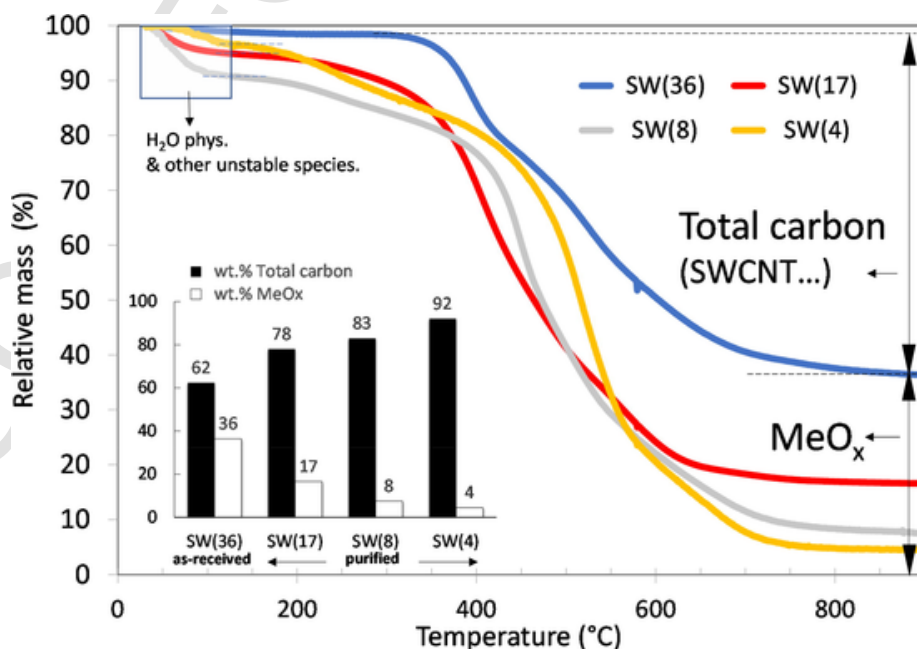

Fig. 2. TGA analysis of the as-received SWCNT (i.e., SW(36)) and after purification in 3 M HNO_3 resulting in SW(17), SW(8) and SW(4) by varying the treatment time. Inset: graphical representation of the MeO_x and total carbon contents derived from the TGA patterns (raw data can be found in Table 1). For clarity, the distribution of total carbon and MeO_x has been indicated for the SW(36) as an example.
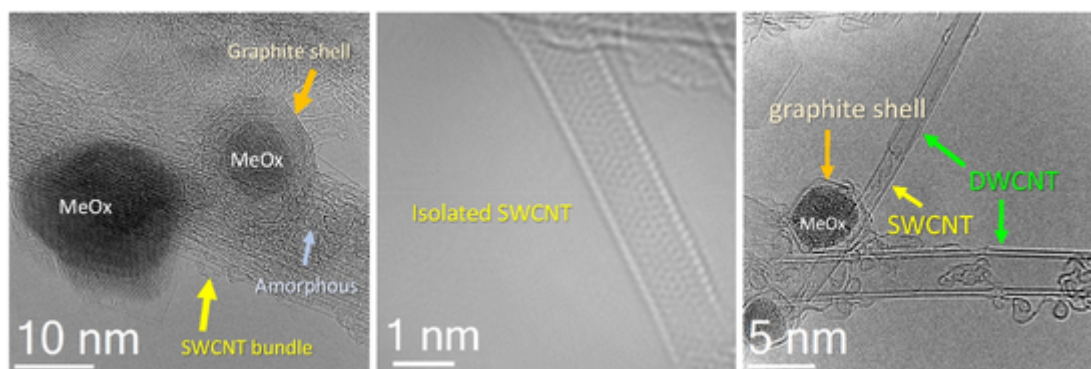
Fig. 3. Cs-corrected high-resolution TEM images for the as-received SWCNT (i.e., SW(36)). Figure S1 displays additional TEM data highlighting the amorphous domains.

Table 1
Compositional and textural properties of the SWCNT materials.

Material	Treatment	MeO$_x$ (%) [a]	Total carbon (%) [b]	S_{BET} (m^2/g)	V_T (cm^3/g)	V_{micro} (cm^3/g) [c]	S_{ext} (m^2/g) [d,e]	S_{micro} (m^2/g) [g]
SW (36)	As-received	36	62	277	uncertain	0.043	175 (-)	102
SW (17)	Purified	17	78	409	0.798	0.087	203 (0.711)	206
SW(8)	Purified	8	83	705	0.670	0.183	255 (0.487)	450
SW(4)	Purified	4	92	127	0.089	0.030	52 (0.059)	75

a) Determined as the residual weight at 900 °C in the TGA patterns.
b) This parameter corresponds to the TGA weight loss between 150 and 900 °C. Total carbon comprises SWCNT, DWCNT, graphite shells and amorphous carbon. The difference 100 – MeO$_x$ – Total carbon (i.e., weight loss between 30 and 150 °C), corresponds to physisorbed water, though other unstable species such as carboxylic groups can count for [47].
c) V_{micro} was determined by the *t*-plot method (Harkins and Jura).
d) S_{ext} is the surface area beyond micropores and it was determined by the *t*-plot method (Harkins and Jura).
e) In parenthesis is the external pore volume, as $V_{ext} = V_T$-V_{micro} (cm^3/g), that is the pore volume beyond micropores.
g) $S_{micro} = S_{BET}$-S_{ext}. Note that the uncertainty on this quantity is related to the BET area in micropores-containing materials and the *t*-plot model.

We did not identify the fraction of SWCNT because for the EB-ODH reaction all types of carbon materials are active, as long as they contain ketonic groups [11–23]. The objectives of this work were focused on the MeO$_x$ removal and oxidative effect on the carbon, by the oxidative and extractive effect of HNO$_3$, and their effects on the catalyst performance.

Besides the MeO$_x$ removal (section 3.2), the HNO$_3$ treatment caused progressive changes in the structure and texture of the carbon. This is firstly discussed with the Raman spectra in Fig. 4. The spectrum of the as-synthesized material (SW(36)) shows the typical features of a SWCNT. The low-frequency peaks are assigned to the A_{1g} symmetry radial breathing mode (RBM). A broad peak at ca. 1340 cm^{-1} called D-band is assigned to disorder; in this case, it comes from the amorphous carbon. Isolated SWCNT can show a D-band which is sharper as compared to the broad band associated to amorphous carbon [50]. A group of peaks in the 1550–1600 cm^{-1} region represents the G-band [51]. This peak is a good measure of the graphitization. In nanotubes, this band splits in two features, G$^+$ (displacement along the nanotube axis) and G$^-$ (circumferential displacement) [50,51]. The G$^-$ band of the SW(36) is formed by two contributions of metallic and semiconducting character, Fig. 4(1). At around 2600 cm^{-1}, an overtone of the D mode is visible, denoted as Ǵ (or D* or 2D). Overall, the RBM bands and splitting of the

G band are distinctive features of the SWCNTs that are visible in the SW(36) material (and eventually for residual DWCNT-rich regions as well).

The shape of the spectra for the purified materials is comparable to that of the as-synthesized SW(36), with the exception of the SW(4). This material has lost the SWCNT character almost entirely; very weak RBM, no splitting of the G region (or very weak G$^-$ bands) and intense D band. This agrees with the textural analysis that displays an isotherm with low porosity (Fig. 5); very different to the SW(36)'s isotherm. Hence, the SW(4) material underwent severe deterioration during the 24 h-HNO$_3$ treatment rendering an amorphous carbon-rich material, also interpreted as very defective graphite, with low porosity. This material can also be understood as a consequence of excessive tube/bundle shortening.

The Raman spectra of SW(17) and SW(8) remain very similar to that of SW(36), proving that those treatments do not modify the structure; their main SWCNT features remain visible (Fig. 4). However, the N$_2$ physisorption isotherms (Fig. 5) reveal some changes on these materials, as compared to the starting SW(36). The adsorption values in the BET region are higher (Fig. 5, rectangle) whereas the pore size distributions shift to lower values (Fig. 5 inset; the tensile strength effect (TSE) is an artifact [52,53] indicating pore neck blocking or to cavitation-induced evaporation). The mesopores in these materials correspond to the space between the SWCNT tubes/bundles (the inner pore size is not visible in the pore size distribution since the diameter is ca. 1 nm, as revealed by TEM in Fig. 3-middle). The shift into smaller mesopore sizes can be understood by the cutting of the SWCNT into smaller assemblies due to the oxidative character of HNO$_3$. Defragmentation of the bundles into thinner ones can occur but it is not obvious if this reduces the void space between bundles, and decreases the pore size. Albeit the Raman spectra did not show severe structural changes for SW(17) and SW(8), as compared to SW(36), the textural analyses indicate a shortening or breaking of the nanotubes/bundles. Shortening/breaking can actually be positive for the reaction since the number of edges increases where the ketonic groups (active sites) are generated by HNO$_3$-induced oxidation. The TSE effect observed for SW(17) and SW(8), Fig. 5 inset, is not very intense but pore restrictions can be present. However, it is not clear where such restrictions are located, in the amorphous domains or in the SWCNT bundle. It is an aspect to keep in mind in the future when studying the deactivation, as pore restrictions can affect the accessibility to active sites when ODH-coke is deposited.

The I$_D$ to I$_{G+}$ ratio, Fig. 4(2), decreases for the SW(17) likely due to the removal by oxidation of the more amorphous carbon domains. This ratio increases for the SW(8) which indicates that defects have increased due to the shortening/breaking of the tubes and newly formed amorphous domains. The high ratio for SW(4) corresponds to a severe amorphization of the material.

The relative intensity of the G$^+$ (axial displacement) to G$^-$ (circumferential displacement) can be used to understand the tube/bundle shortening/breaking as well. The relative intensity of G$^+$ band to the G$^-$
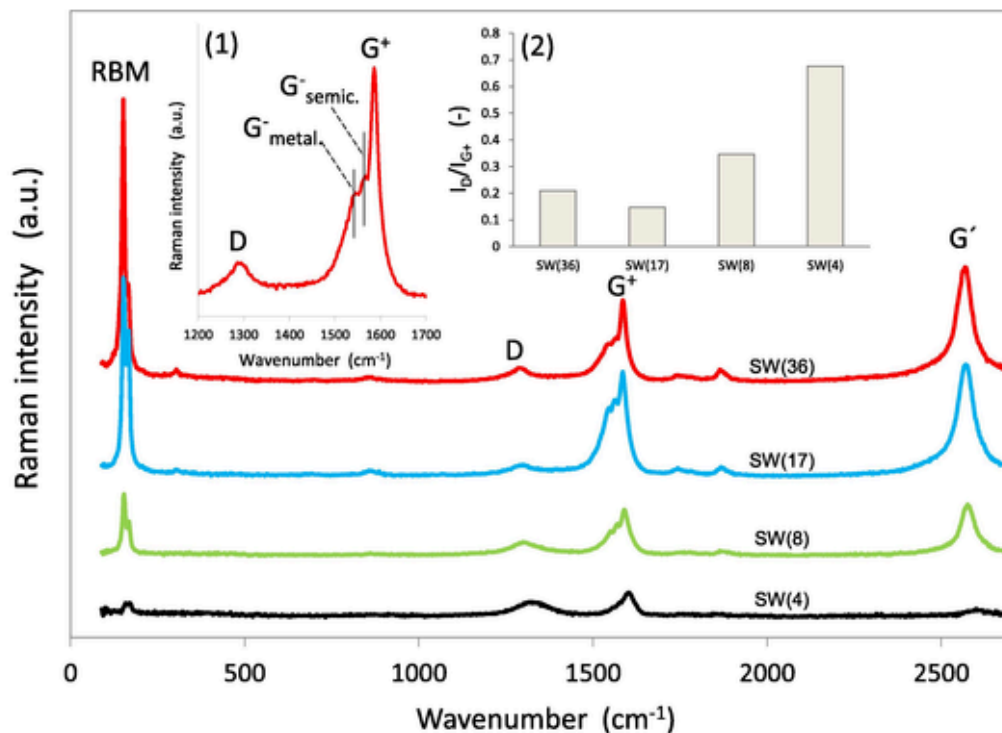
Fig. 4. Characterization of the SWCNT materials by Raman. Inset (1): amplification of the G region including the band assignments. Inset (2): representation of the I_D to I_{G+} ratio.
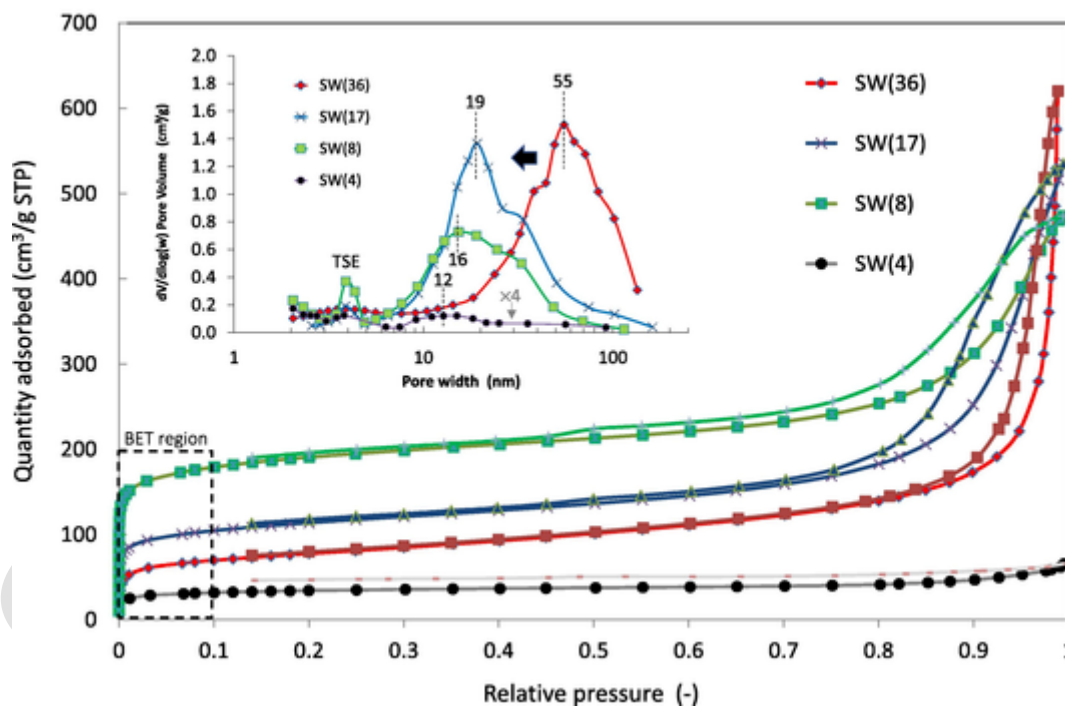

Fig. 5. Characterization of the SWCNT materials by nitrogen sorption at −196 °C. Inset: BJH pore size distribution of the desorption branches.

bands is smaller for the SW(17) and SW(8), as compared to the SW(37). As the diameter of the tube does not change during the purification, the G^+/G^- change means that the axial displacement is reduced. This is in agreement with the shortening/cutting of the tubes/bundles, as discussed earlier by the smaller mesopores. It must be kept in mind that

the G^+ band intensity can decrease when the SWCNT sidewall is functionalized [54]. However, the HNO_3 treatment does not functionalize the sidewall.

The textural parameters BET area, microporous and external surface areas increased upon purification (Table 1). The increase is ascribed to

the formation of smaller pores that contribute more to the microporosity and mesoporosity, but also to the MeO$_x$ removal. The MeO$_x$ particles are non-porous and heavier than the carbon itself, so they have a diluting effect in the surface areas. In other words, the denominator (i.e., weight) gets lower when MeO$_x$ is removed, and the textural parameters increase. A deviation from the trend was observed for SW(4) due to the severe deterioration of the material during the treatment, leading to a low porous carbon containing micro- and small mesopores. The pore size distribution shows a very weak peak at ca. 12 nm, the smallest in the series (Fig. 5 inset). NLDFT calculations in Figure S2 indicate that nearly half of its pore volume is taken up in the microporous region and its relative contribution of mesoporous volume is much smaller than the other materials.

The shortening/cutting of the tubes/bundles was suggested earlier as beneficial since having more edges would accommodate more active sites; i.e., C=O groups. This was assessed by the O1s XPS analysis (Figure S3). Each spectrum was deconvoluted into four components, corresponding to C=O (ketonic carbonyl groups), O=C-O (sum of carboxylic acid, anhydride, lactone, and ester groups), C-OH (phenol groups) and water [43]. Quantitative results (Table 2) reveal that the C=O concentration increases in about 60 % on average for all purified

Table 2
XPS carbon–oxygen-based surface species (% at) from the O1s spectra deconvolution.[a,b] Spectra can be found in Figure S3.

Material	[C=O] (% at.) at 531.3 eV	[O=C-O] (% at.) at 532.5 eV	[C-OH] (% at.) at 533.8 eV
SW(36)	0.91	4.38	5.07
SW(17)	1.53	3.84	2.59
SW(8)	1.49	4.33	3.74
SW(4)	1.40	3.38	3.10

a) The deconvolution was done based on Qi et al. [43]. See additional explanation in section 2.4.
b) The surface contribution of MeO$_x$ was small (Table S3) and it was present as reduced species (data not shown). Moreover, there was no visible shoulder at 528–530 eV in Figure S3 due to possible Me-O, therefore the O 1S signal was entirely assigned to organic O-carbon species.

materials; no significant changes among the treated materials were observed. The other O-containing species do not increase upon treatment.

Differences in the O/C ratio of the purified samples were also observed (Table S3). The starting material contains a large fraction of surface oxygen (O/C = 0.14). The presence of oxygen species in the as-grown SWCNT was also observed by Martínez et al. [55]. The purified materials contain less surface oxygen (O/C between 0.10 and 0.12) than the non-purified one, but the O-species are different. The oxidative purification renders more ketonic species as explained above, which is beneficial for the reaction.

Overall, the HNO$_3$-based treatment triggered two effects: carbon surface oxidation and MeO$_x$ dissolution. The MeO$_x$ is dissolved, likely after oxidation of the more amorphous covering carbon-layer, whereas the MeO$_x$ covered by graphitic carbon is more stable to HNO$_3$ oxidation. Nevertheless, some of these graphitic domains can have defects and holes, through where HNO$_3$ can penetrate and dissolve MeO$_x$. Lowering the MeO$_x$ content by longer treatment times (e.g. 24 h) was found to be detrimental since the structure gets amorphous, or very defective, and the MeO$_x$ concentration does not decrease much further. Thus, it remains a challenge to lower the MeO$_x$ concentration by this method while maintaining the SWCNT structure. On the other hand, shorter processing times diminish the MeO$_x$ concentration, the SWCNT structure is preserved and the concentration of surface C=O groups increases due to the oxidative treatment on the edges.

3.4. Catalyst performance and additional characterization

The catalytic tests were carried out at equal catalyst bed volume to mimic a real situation where the reactor volume is given or limiting [23,25–30,56], rather than constant catalyst weight. This is particularly useful for revamping an existing unit. But for new reactors, it accounts for the catalyst density that sometimes is very low, leading to excessively large reactor volumes that cannot be implemented. Thus, constant volume provides a more realistic comparison of the catalytic data towards implementation for this reaction.

Fig. 6 compiles the catalyst performance results. The reaction was carried out at 350 °C to avoid full O$_2$ conversion. Melián-Cabrera and Zarubina [56] showed that under complete O$_2$ conversion, the selec-
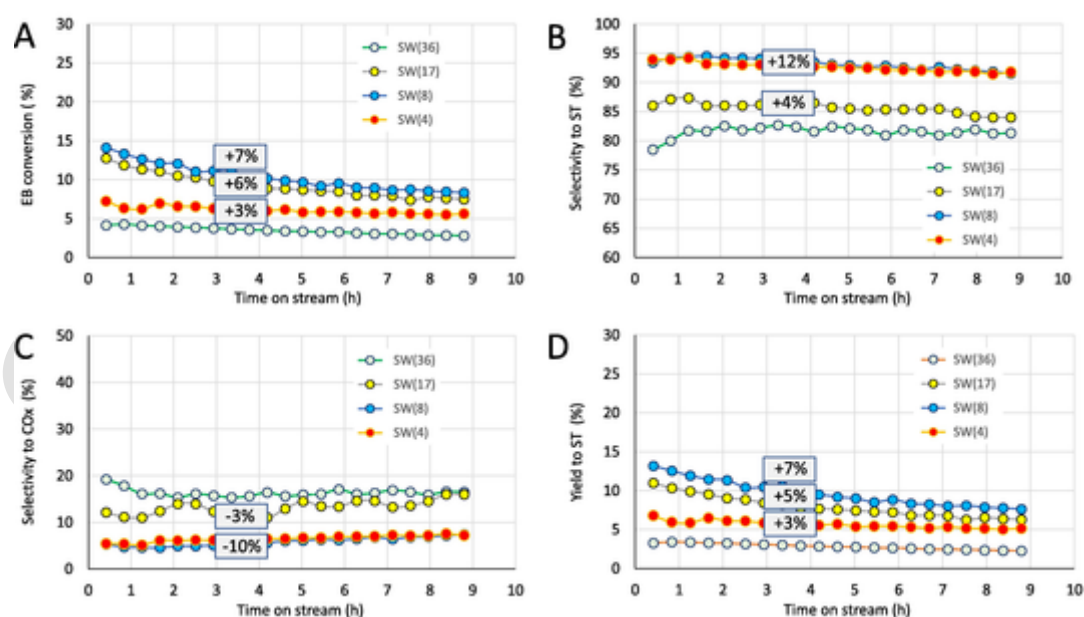

Fig. 6. Catalytic performance parameters versus time on stream for various SWCNT materials, fresh and purified, for the EB-ODH reaction: **A)** EB conversion, **B)** selectivity to styrene (ST), **C)** selectivity to CO$_x$ and **D)** yield to styrene. Reaction conditions: 350 °C, O$_2$/EB = 0.6 (vol.); GHSV of 2700 l/h/l; 10 vol% EB. The highlighted values on the lines correspond to the absolute increase with respect to the SW(36), of the 9 h-run averaged data.

tivity and conversion are linked. This was confirmed afterwards by Mercadal et al. [57]. Particularly, the EB conversion is determined by the selectivity to CO_x. Therefore, under complete O_2 conversion (i.e., $X_{O_2} = 100\%$) the catalyst performance interpretation is limited to selectivity only. The trade-off of this approach is the low EB conversion. However, this can be enhanced by operating at a higher temperature or higher WHSV, or both, in a different type of optimization study. This work aims at assessing the impact of the purified SWCNTs on the conversion and selectivities. The only way to do that is by working at incomplete O_2 conversion (i.e., $X_{O_2} < 100\%$).

The purification shows a positive effect on the EB conversion (Fig. 6A), with the exception of SW(4) that is discussed later. The purification brings also positive selectivity changes; the ST selectivity increases (Fig. 6B) whereas that for CO_x decreases (Fig. 6C). The framed values in the graphs correspond to the absolute increase (+) or decrease (-) with respect to the SW(36) as reference case, after averaging the 9 h-run data. The increase in styrene selectivity nearly matches the decrease in CO_x. This matching infers that these products are formed in competitive routes. The purification enhanced both EB conversion and ST selectivity in the series but it fails at the most purified catalyst, SW(4); the selectivity is high but the conversion drops. Considering the ST yield (Fig. 6D) the optimal catalyst is SW(8). When the separation of by-products is troublesome, selectivity is preferred than yield in the optimization. In this case, both parameters are optimal for SW(8). However, this is a relative optimum. Other optimal composition/s may be found by further investigation. Such optimization can be done using this or other purification approaches. The challenge is to lower the MeO_x concentration while keeping the SWCNT structure and having more C═O sites.

The drop of the EB conversion (X_{EB}) with time on stream (TOS) for SW(17) and SW(8), Fig. 6A, can be ascribed to the deposition of the ODH-coke, which lowers the surface area. The ODH-coke, formed during the reaction, is also a catalyst for this reaction as it contains ketonic groups, yet the surface area of the system 'ODH-coke/SWCNT' decreases due to fouling [57]. This would impact negatively on the conversion since there are less accessible sites. Note that surface area did not play a role in previous studies [56,57] due to the fact that O_2 was fully converted, and the EB conversion was determined by the CO_x selectivity. In other words, the effect of fouling on X_{EB} is visible when $X_{O_2} < 100\%$, otherwise (i.e., $X_{O_2} = 100\%$) the selectivity to CO_x determines X_{EB}. In the coming discussion, we will rationalize the improvements in conversion, selectivity and, finally, yield.

The enhanced EB conversion can be first ascribed to the changes previously discussed on the material intrinsic properties: enhanced textural features (shortening of the tubes/bundles, and removal of MeO_x) and therefore more surface C═O sites. The shortening of the tubes/bundles creates more edges where active sites can be located. Secondly, we operated at fixed reactor bed volume and there is a higher catalyst weight load in the reactor upon MeO_x removal (Table S2). The EB conversion enhancement is hence the result of multiple effects; material-intrinsic and weight-based factors. This can be quantified using the C═O sites in the catalyst bed using the O1s XPS data. The amount of

Table 3

Species contents in the catalyst bed derived from XPS data. Section 2.4 provides more information about the employed approach.

Material	[C═O] (μmol/bed) [a] at 531.3 eV	[C-OH] (μmol/bed) [b] at 533.8 eV	[C═O] + [C-OH] (μmol/bed)
SW (36)	44	246	290
SW (17)	203	345	548
SW(8)	218	545	763
SW(4)	428	948	1376

a. Values calculated as: $[C = O] \left(\frac{mol}{bed} \right) \approx M \left(\frac{mol\ carbon\ material}{bed} \right) \times \frac{[C=O](\%at.)}{100}$ where M was calculated using an average molecular weight of the material considering C and O only (Table S3), whose concentrations are higher than 97 %. The [C═O] values are given in Table 2.

b. Values calculated as: $[C - OH] \left(\frac{mol}{bed} \right) \approx M \left(\frac{mol\ carbon\ material}{bed} \right) \times \frac{[C-OH](\%at.)}{100}$. M is explained in footnote **a**. The [C-OH] values are given in Table 2.

ketonic carbonyl in the bed can be calculated following the equations given in Table 3, where the average molecular weight was calculated from the XPS O and C % only (C + O > 97 %, Ni + Y < 1 %, Table S3). Albeit this quantity, μmol C═O/bed, provides an approximation to the number of active sites in the bed. The actual sites have been claimed to be diketones under a certain proximity to activate the ethyl group [9,10,12,58]. However, those sites remain difficult to quantify, so we will be using the above figure as an approximation. The so-calculated values increase with the purification treatment (Fig. 7A). The representation of the initial EB conversion versus this parameter in Fig. 7B follows a lineal trend; the EB conversion increases with the number of surface C═O sites in the bed. In this case, the initial conversions were used as the XPS data were obtained from the fresh catalysts. Therefore, the improvement in EB conversion can be ascribed to the improved intrinsic properties of the materials after purification (i.e., more surface C═O), as well as the higher weight load in the catalyst bed.

Interestingly, the same approach was done by quantifying the C-OH groups, with the final values represented in Fig. 7A (raw data in Table 3). The amount of C-OH in the catalyst bed also increases. This effect is not intrinsic (cf. values in Table 2), but it comes from the higher weight load. Fig. 7B also represents the initial EB conversion versus the sum of C═O + C-OH and an increasing trend was obtained as for the C═O sites alone. These results indicate that both sites can be considered in the mechanistic interpretation. It can be explained in two ways. First, it is likely that the C-OH groups are oxidized during the reaction forming ketonic groups and engage in the mechanism. Secondly, the active site model comprises both ketonic and phenol groups as a redox pair (C═O ⇆ C-OH) [9,10,58], therefore it is sensible to consider both functional groups. However, the role of the C-OH in this reaction has been generally overlooked. Our results indicate that C-OH can play a
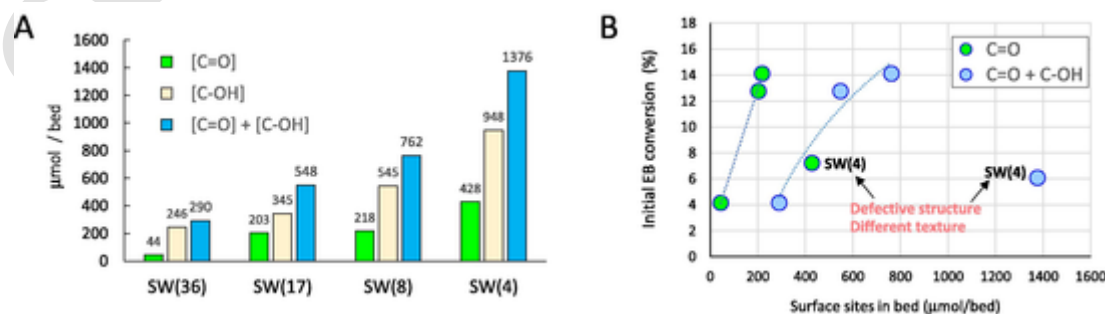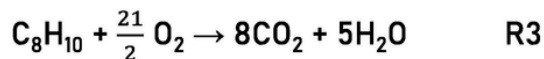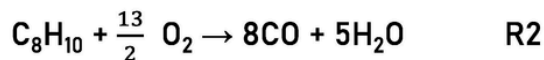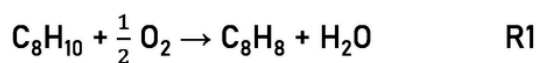

Fig. 7. A) Amount of C═O and C-OH as determined by XPS (raw data in Table 3). **B)** Representation of the initial EB conversion as a function of the surface groups, C═O, or the sum C═O + C-OH. The trending lines are meant to guide the eye.

role in the interpretation as well. The main fundamental problem is that the actual catalytic pairs are those in close proximity to activate the ethyl group, and such species remain difficult to quantify. It is relevant to note here that the interpretation of the performance of oxygen functionalization in carbon materials is often overlooked on behalf of other heteroatoms (mainly nitrogen); this has been recently reviewed [59]. Though we have shown that C-OH can play a role in the interpretation, an additional experimental proof is required. The forthcoming discussion will be focused on C=O only, as these sites have been proposed in several studies on different materials, including characterization but also *in-situ* titration during the reaction of the C=O groups [60,61].

There is one catalyst, SW(4), that does not follow the trends in Fig. 7B. This catalyst contains a large loading of C=O in the bed, but the EB conversion was lower than expected by the trend line. There are a few ways to rationalize this result. One is that the amount of C=O sites is high but the true sites under a certain proximity (specific diketones) is lower due to the carbon structural differences in SW(4), i.e., more amorphous or defective carbon. Another explanation can be found in the redox mechanism; the active site regeneration of C-OH into C=O via O_2 activation can be hindered in such an amorphous structure as compared to a carbon nanotube. In other words, an amorphous or very defective carbon structure may hinder the O_2 activation. Note that the O_2 activation in this reaction is ill understood [10]. Thirdly, and finally, the porosity of this material can be a handicap, formed by small mesopores and micropores. Here two explanations are thinkable. It may be possible that some active sites are located in micropores that are not accessible to EB and therefore they do not participate in the reaction. This can be interpreted as having a lower number of active sites running the reaction, lower that those quantified by XPS. Or, as another explanation, EB is accessible but diffuses slower (activated diffusion) in such smaller pores. In this scenario, two regimes can coexist in the catalyst; a kinetically-controlled regime in wide pores as compared to small pores where there would be an activated diffusion of EB. If the problem lays on the slower ST diffusivity in this catalyst, then a drop in selectivity would be expected since CO_x is much smaller. However, the selectivity does not drop. It remains high, comparable to SW(8). Thus, if diffusivity is troublesome, this should be on EB. This scenario is even more complex to explain quantitatively because the reactivity of each site (those in wide pores and in smaller pores) would differ. But, in qualitative terms, the fact that a fraction is under diffusion control can explain the lower overall conversion.

The interpretation of the selectivity is more complex than the conversion. It can be first interpreted in similar terms as conversion. As there are more surface C=O active sites in the bed catalyzing the main reaction, more styrene is formed. In other words, O_2 reacts favourably through R1 (Fig. 8) and the CO_x-forming routes (R2 and *R*3, in Fig. 8) that compete for O_2 are inhibited. Therefore, the CO_x selectivity drops and ST increases. Note that styrene is stable in the presence of O2 [27], meaning that the routes R4 and R5 (Fig. 8) are unlikely to occur (i.e., CO_x formation via styrene). The selectivity interpretation can include other effects. We observed by TEM that the residual MeO_x were covered by a graphitic layer before the reaction (Fig. 9A, occasionally the layer
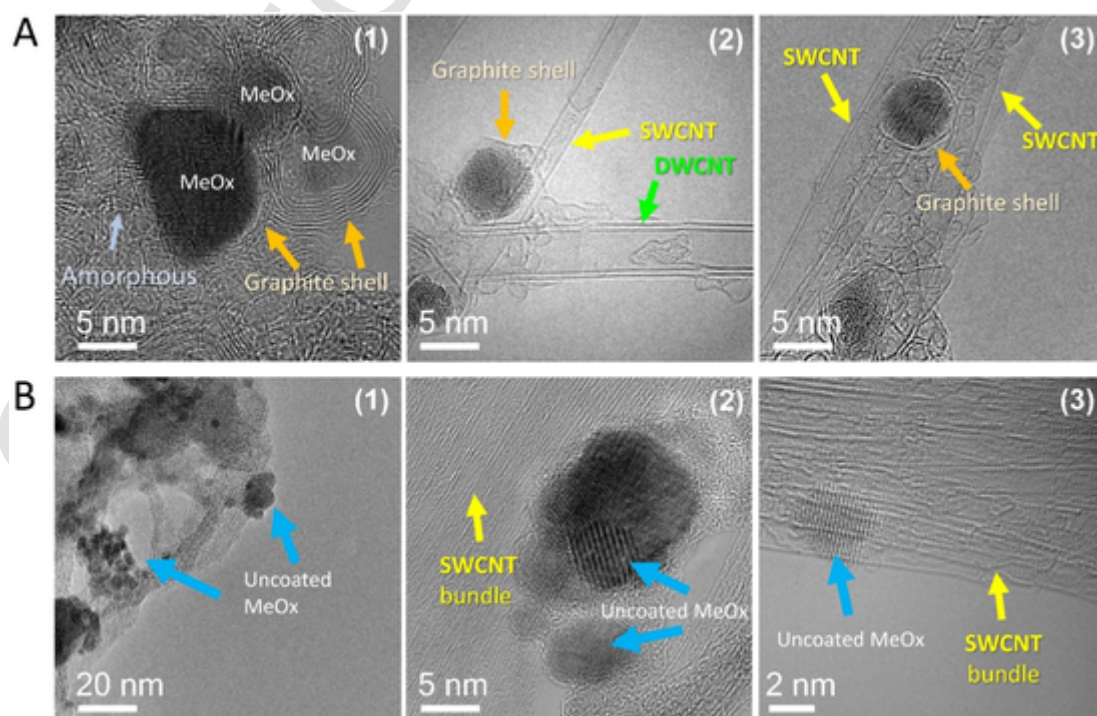
Macroscopic reactions

$$C_8H_{10} + \tfrac{1}{2}\,O_2 \rightarrow C_8H_8 + H_2O \qquad \text{R1}$$

$$C_8H_{10} + \tfrac{13}{2}\,O_2 \rightarrow 8CO + 5H_2O \qquad \text{R2}$$

$$C_8H_{10} + \tfrac{21}{2}\,O_2 \rightarrow 8CO_2 + 5H_2O \qquad \text{R3}$$

Other possible internal pathways

$$C_8H_8 + 6\,O_2 \rightarrow 8CO + 4H_2O \qquad \text{R4}$$

$$C_8H_8 + 10\,O_2 \rightarrow 8CO_2 + 4H_2O \qquad \text{R5}$$
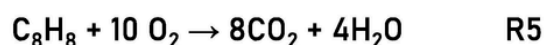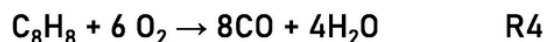
Fig. 8. Reactions taking place during the EB-ODH process.

Fig. 9. Cs-corrected high-resolution TEM images of the purified SW(8): **A)** fresh and **B)** after the reaction. The different types of structures are indicated in the images.

was amorphous as seen in Figure S1). But such carbon layers disappear during the reaction (Fig. 9B), rendering uncoated MeO_x particles. Such uncoated particles can catalyse the CO_x formation and consequently drops the styrene selectivity, as both routes compete. Therefore, by lowering the MeO_x content along the purified series, its CO_x-forming effect in the reaction can be diminished (forming more styrene).

At the moment, there are two positive parameters contributing to the C꞊O in the bed; catalyst loading and intrinsic C꞊O in the materials, both are enhanced with the purification. But there can be a MeO_x effect that is masked; it could contribute to CO_x formation and therefore lowering the styrene synthesis. This MeO_x effect cannot be deduced from these experiments because the C꞊O and MeO_x loadings per bed vary in the series. The MeO_x role could be studied by preparing catalysts with equal C꞊O and variable MeO_x loadings in the bed. However, this is not a trivial task as it requires a laborious sample preparation approach. Then, we would be able to know if MeO_x has an effect on CO_x formation and lowering styrene synthesis. In other words, with that information we would know if the here-presented effect is due to a single contribution (having more O-functionalized carbon in bed) or two contributions (more O-functionalized carbon and less detrimental MeO_x in bed). In the eventual case that MeO_x would have a positive effect in forming styrene, our results imply that the O-functionalised carbon is a better catalyst.

The interpretation of the steady-state performance (i.e., after 9 h time on stream) would require characterising the after-reaction catalysts. This is because the reaction produces *in situ* ODH-coke that has been claimed to catalyze the reaction as well [23,25–30,56–58]. This makes understanding the deactivation even more difficult, as compared to a conventional coke deposited on active sites. The study of the deactivated catalysts is out of the scope of the present study.

Calculation of the intrinsic styrene yield per cm^3 of catalyst (Fig. 10A, average values) shows clearly the effect of purification. In the optimal catalyst, the increase is nearly 240 % higher due to both conversion and selectivity increase; ultimately due to both higher load of carbon in the bed and improved intrinsic properties (surface C꞊O sites). When the structure gets defective, SW(4), the conversion decreases with a pronounced drop in the yield. An interesting observation is

found when the yield is referenced to the amount of carbon (Fig. 10B, average values). The catalysts keeping the SWCNT structure give high values. But the more defective catalyst, SW(4), gives a much lower yield per carbon basis. This points into a different mechanism taking place in this material; less diketones, O_2 activation can be hindered in a more amorphous carbon, or inaccessible/diffusion-controlled active sites, as discussed earlier to explain the conversion, since its selectivity was high.

Discussing the intrinsic yield at the beginning of the reaction, without deactivation, is more appropriate for a correlation with the catalyst properties, done on the fresh catalysts. The purified catalysts keeping the SWCNT structure, i.e., SW(17) and SW(8), show higher intrinsic styrene yield compared to the non-purified SW(36), Fig. 11A. The differences can be attributed to the improved functionalisation and texture of the purified SWCNT catalysts. The intrinsic yield decreases with time of stream (Fig. S4B) and at the end of the run, it is pretty similar among the good catalysts, i.e., SW(36), SW(17) and SW(8). The end values have been plotted in Fig. 11A so they can be compared to the initial ones. The comparison indicates that initially the performance is dominated by the intrinsic properties of the SWCNT, whilst at the end, the deactivation flattens the differences. The values of the good catalysts end up pretty similar; a possible explanation can be the deposition of ODH-coke, which is also active, and dominates the intrinsic yield at the end of the run. However, other phenomena cannot be ruled out. A similar situation is seen in the volumetric yield (Fig. 11B) that is maximal at the beginning in the absence of deactivation. At the end, the volumetric yield of the purified catalysts is still higher than the non-purified; this effect is mainly due to the higher volumetric catalyst loading in the reactor as the intrinsic yield were more comparable among them. Importantly, the above comparison makes it clear that to maximize the purification effect on the intrinsic and volumetric yields, the deactivation needs to be avoided or minimized.

There are few ways to improve further the performance. One is to minimize the MeO_x loading, adding C꞊O groups, and keeping the SWCNT structure by this or other purification strategy. In addition, the process rendered amorphous or very defective carbon domains during the HNO_3 treatment. Removing the amorphous carbon can be useful to
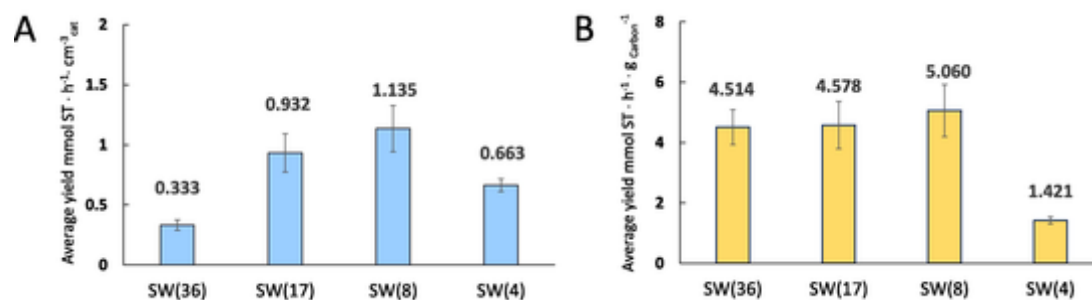

Fig. 10. A) Average styrene yield per cm^3 of catalyst. **B**) Average styrene yield per gram of carbon. Bars correspond to the standard deviation; this does not represent error but deviation due to deactivation as shown in Figure S4.
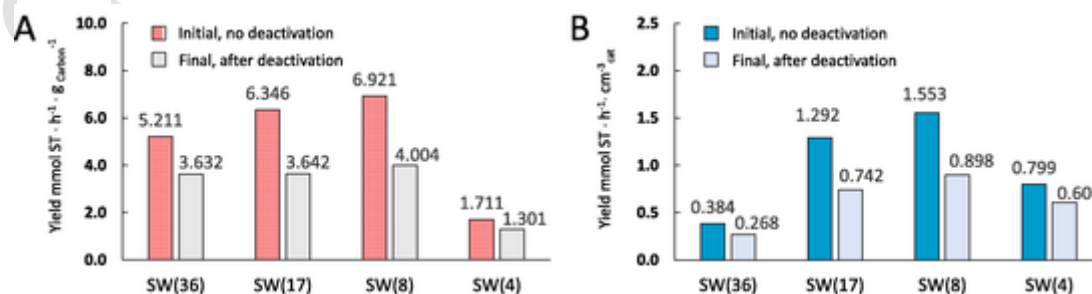

Fig. 11. A) Styrene yield per gram of carbon, initial and final. **B**) Styrene yield per cm^3 of catalyst, initial and final. Data can be found in Figure S4.

understand the role of this on the catalyst performance. All these topics are interesting fundamentally, but studying the deactivation mechanism (e.g. ODH-coke deposition) to maximize the SWCNT performance is perhaps more critical.

A comparison of these results with the literature is difficult because of the different applied reaction conditions. We specifically employed industrially relevant conditions: limited O_2, high EB concentration and a high WHSV. Other studies usually employ low EB concentrations, a huge excess of O_2 and low WHSV, likely to enhance the EB conversion but at conditions that are not practical, as discussed in the Introduction. Among the various parameters, selectivity is perhaps the most critical one in the EB-ODH, since the by-product CO_x has no value. Therefore, the lower operational temperature for EB-ODH, as compared to the conventional process, is not benefited if the selectivity towards CO_x is high. Our results can however be compared to a previous study [23]. In that study, various carbon-based materials were evaluated under similar reaction conditions. Those carbon-based materials yielded a selectivity to styrene ranging between 70 and 90 %, whereas the optimal SWCNT of this work yielded a selectivity around 92–95 %. This is an important improvement since the selectivity of this reaction is a major limitation for implementation [2]. Conversion was not targeted in this study and it remains an open topic for this type of catalysts that can be enhanced by WHSV (e.g. O_2 stage feeding with more catalyst) and temperature by considering the thermal stability of the catalyst. In this sense, SWCNT should be operated at moderate temperatures.

4. Conclusions

A raw SWCNT prepared by arc discharge was purified by processing it in a HNO_3 solution for different periods of time. This rendered metal-purified and surface-oxidized SWCNTs, featuring lower MeO_x contents and higher concentration of surface C=O. The treatment generally preserved the SWCNT structure and led to improvements of the textural features, ascribed to the cutting of the tubes/bundles by oxidation and removal of the MeO_x. The treatment was very positive in the oxidative dehydrogenation of ethylbenzene: ethylbenzene conversion increased, selectivity towards styrene increased and undesirable CO_x decreased. Catalyst performance and characterization data were correlated at the beginning of the reaction, since fresh catalysts were characterized. The conversion was interpreted by the improvement of the intrinsic properties and to the higher catalyst load in the bed upon MeO_x removal, both lead to higher styrene-forming C=O sites in the bed. The selectivity was interpreted by the higher number styrene-forming C=O sites in the bed, albeit the possible catalytic role of uncoated MeO_x in CO_x formation (thereby decreasing styrene synthesis), could not be ruled out. The styrene yield per catalyst volume was improved in ca. 240 % on average as compared to the non-purified SWCNT. To maximize the purification effect on the intrinsic and volumetric yields, the deactivation needs to be avoided or minimized. Importantly, an extensive purification treatment resulted into a defective graphitic structure and worse conversion and yield, intrinsic per gram of carbon and volumetric. Therefore, the purification should preserve the SWCNT structure to maximize the performance. Overall, this method proved to be very positive with remarkable performance improvements, on the selectivity and yield. In terms of the purification method, a trade-off was found; the higher the MeO_x is removed, the more defective the SWCNT becomes.

Declaration of Competing Interest

The authors declare that they have no known competing financial interests or personal relationships that could have appeared to influence the work reported in this paper.

Data availability

Data will be made available on request.

Appendix A. Supplementary data

Supplementary data to this article can be found online at https://doi.org/10.1016/j.cej.2022.140723.

References

[1] E. Lam, J.H.T. Luong, Carbon materials as catalyst supports and catalysts in the transformation of biomass to fuels and chemicals, ACS Catal. 10 (2014) 3393–3410.
[2] I. Melián-Cabrera, Catalytic materials: concepts to understand the pathway to implementation, Ind. Eng. Chem. Res. 60 (2021) 18545–18559.
[3] F. Rodríguez-Reinoso, The role of carbon materials in heterogeneous catalysis, Carbon 36 (1998) 159–175.
[4] V. Budarin, J.H. Clark, J.J.E. Hardy, R. Luque, K. Milkowski, S.J. Tavener, A.J. Wilson, Starbons: new starch-derived mesoporous carbonaceous materials with tunable properties, Angew. Chem. Int. Ed. 45 (2006) 3782–3786.
[5] M. Seredych, D. Hulicova-Jurcakova, G.Q. Lu, T.J. Bandosz, Surface functional groups of carbons and the effects of their chemical character, density and accessibility to ions on electrochemical performance, Carbon 46 (2008) 1475–1488.
[6] P. Serp, B. Machado, Nanostructured Carbon Materials for Catalysis, Royal Society of Chemistry, Cambridge, UK, 2015.
[7] X. Liu, L. Dai, Carbon-based metal-free catalysts, Nat. Rev. Mat. 1 (2016) 16064.
[8] W. Kiciński, S. Dyjak, Transition metal impurities in carbon-based materials: Pitfalls, artifacts and deleterious effects, Carbon 168 (2020) 748–845.
[9] Y. Iwasawa, H. Nobe, S. Ogasawara, Reaction mechanism for styrene synthesis over polynaphthoquinone, J. Catal. 31 (1973) 444–449.
[10] W. Qi, P. Yan, D.S. Su, Oxidative dehydrogenation on nanocarbon: insights into the reaction mechanism and kinetics via in situ experimental methods, Acc. Chem. Res. 51 (2018) 640–648.
[11] G.C. Grunewald, R.S. Drago, Oxidative dehydrogenation of ethylbenzene to styrene over carbon-based catalysts, J. Mol. Catal. 58 (1990) 227–233.
[12] M.F.R. Pereira, J.J.M. Orfão, J.L. Figueiredo, Oxidative dehydrogenation of ethylbenzene on activated carbon catalysts. I. Influence of surface chemical groups, Appl. Catal. A: Gen. 184 (1999) 153–160.
[13] N. Keller, N.I. Maksimova, V.V. Roddatis, M. Schur, G. Mestl, Y.V. Butenko, V.L. Kuznetsov, R. Schlögl, The catalytic use of onion-like carbon materials for styrene synthesis by oxidative dehydrogenation of ethylbenzene, Angew. Chem. Int. Ed. 41 (2002) 1885–1888.
[14] D.S. Su, N.I. Maksimova, G. Mestl, V.L. Kuznetsov, V. Keller, R. Schlögl, N. Keller, Oxidative dehydrogenation of ethylbenzene to styrene over ultra-dispersed diamond and onion-like carbon, Carbon 45 (2007) 2145–2151.
[15] G. Mestl, N.I. Maksimova, N. Keller, V.V. Roddatis, R. Schlögl, Carbon nanofilaments in heterogeneous catalysis: an industrial application for new carbon materials? Angew. Chem. Int. Ed. 40 (11) (2001) 2066–2068.
[16] T.J. Zhao, W.Z. Sun, X.Y. Gu, M. Rønning, D. Chen, Y.C. Dai, W.K. Yuan, A. Holmen, Rational design of the carbon nanofiber catalysts for oxidative dehydrogenation of ethylbenzene, Appl. Catal. A: Gen. 323 (2007) 135–146.
[17] J. Diao, Z. Feng, R. Huang, H. Liu, S. Bee, A. Hamid, D.S. Su, Selective and stable ethylbenzene dehydrogenation to styrene over nanodiamonds under oxygen-lean conditions, ChemSusChem 9 (2016) 662–666.
[18] L. Wang, J. Zhang, D.S. Su, Y. Ji, X. Cao, F.S. Xiao, Simple preparation of honeycomb-like macrostructured and microporous carbons with high performance in oxidative dehydrogenation of ethylbenzene, Chem. Mater. 19 (2007) 2894–2897.
[19] D.S. Su, J.J. Delgado, X. Liu, D. Wang, R. Schlögl, L. Wang, Z. Zhang, Z. Shan, F.S. Xiao, Highly ordered mesoporous carbon as catalyst for oxidative dehydrogenation of ethylbenzene to styrene, Chem. Asian J. 4 (2009) 1108–1113.
[20] L. Wang, J.J. Delgado, B. Frank, Z. Zhang, Z. Shan, D.S. Su, F.S. Xiao, Resin-

derived hierarchical porous carbon spheres with high catalytic performance in the oxidative dehydrogenation of ethylbenzene, ChemSusChem 5 (2012) 687–693.

[21] M.F.R. Pereira, J.L. Figueiredo, J.J.M. Orfão, P. Serp, P. Kalck, Y. Kihn, Catalytic activity of carbon nanotubes in the oxidative dehydrogenation of ethylbenzene, Carbon 42 (2004) 2807–2813.

[22] J. Zhang, D.S. Su, A. Zhang, D. Wang, R. Schlögl, C. Hebert, Nanocarbon as robust catalyst: mechanistic insight into carbon-mediated catalysis, Angew. Chem. Int. Ed. 46 (2007) 7319–7323.

[23] V. Zarubina, H. Talebi, C. Nederlof, F. Kapteijn, M. Makkee, I. Melian-Cabrera, On the stability of conventional and nano-structured carbon-based catalysts in the oxidative dehydrogenation of ethylbenzene under industrially relevant conditions, Carbon 77 (2014) 329–340.

[24] F. Cavani, F. Trifiro, Alternative processes for the production of styrene, Appl. Catal. A 133 (1995) 219–239.

[25] C. Nederlof, V. Zarubina, I. Melián-Cabrera, H.J. Heeres, F. Kapteijn, M. Makkee, Oxidative dehydrogenation of ethylbenzene to styrene over alumina: effect of calcination, Catal. Sci. Technol. 3 (2) (2013) 519–526.

[26] V. Zarubina, C. Nederlof, B. van der Linden, F. Kapteijn, H.J. Heeres, M. Makkee, I. Melián-Cabrera, Making coke a more efficient catalyst in the oxidative dehydrogenation of ethylbenzene using wide-pore transitional aluminas, J. Mol. Catal. A-Chem. 381 (2014) 179–187.

[27] C. Nederlof, V. Zarubina, I. Melián-Cabrera, H.J. Heeres, F. Kapteijn, M. Makkee, Application of staged O_2 feeding in the oxidative dehydrogenation of ethylbenzene to styrene over Al_2O_3 and P_2O_5/SiO_2 catalysts, Appl. Catal. A: Gen. 476 (2014) 204–214.

[28] C. Nederlof, P. Vijfhuizen, V. Zarubina, I. Melián-Cabrera, F. Kapteijn, M. Makkee, A TEOM investigation on coke formation in the oxidative dehydrogenation of ethylbenzene to styrene, Catal. Sci. Technol. 4 (2014) 3879–3890.

[29] V. Zarubina, H. Talebi, H. Jansma, K. Góra-Marek, C. Nederlof, F. Kapteijn, M. Makkee, I. Melián-Cabrera, On the thermal stabilization of carbon-supported SiO_2 catalysts by phosphorus: evaluation in the oxidative dehydrogenation of ethylbenzene to styrene and a comparison with relevant catalysts, Appl. Catal. A: Gen. 514 (2016) 173–181.

[30] I. Melián-Cabrera, V. Zarubina, C. Nederlof, F. Kapteijn, M. Makkee, An in situ reactivation study reveals the supreme stability of γ-alumina for the oxidative dehydrogenation of ethylbenzene to styrene, Catal. Sci. Technol. 8 (2018) 3733–3736.

[31] H. Hu, B. Zhao, M.E. Itkis, R.C. Haddon, Nitric acid purification of single-walled carbon nanotubes, J. Phys. Chem. B 107 (2003) 13838–13842.

[32] P.X. Hou, C. Liu, H.M. Cheng, Purification of carbon nanotubes, Carbon 46 (2008) 2003–2025.

[33] M. Pumera, Carbon nanotubes contain residual metal catalyst nanoparticles even after washing with nitric acid at elevated temperature because these metal nanoparticles are sheathed by several graphene sheets, Langmuir 23 (2007) 6453–6458.

[34] I.W. Chiang, B.E. Brinson, R.E. Smalley, J.L. Margrave, R.H. Hauge, Purification and characterization of single-wall carbon nanotubes, J. Phys. Chem. B 105 (2001) 1157–1161.

[35] I.W. Chiang, B.E. Brinson, A.Y. Huang, P.A. Willis, M.J. Bronikowski, J.L. Margrave, R.E. Smalley, R.H. Hauge, Purification and characterization of single-wall carbon nanotubes (SWNTs) obtained from the gas-phase decomposition of CO (HiPco Process), J. Phys. Chem. B 105 (2001) 8297–8301.

[36] W. Huang, Y. Wang, G.H. Luo, F. Wei, 99.9% purity multi-walled carbon nanotubes by vacuum high-temperature annealing, Carbon 41 (2003) 2585–2590.

[37] M. Yudasaka, H. Kataura, T. Ichihashi, L.-C. Qin, S. Kar, S. Iijima, Diameter enlargement of HiPco single-wall carbon nanotubes by heat treatment, Nano Lett. 1 (9) (2001) 487–489.

[38] M. Thommes, K. Kaneko, A.V. Neimark, J.P. Olivier, F. Rodriguez-Reinoso, J. Rouquerol, K.S.W. Sing, Physisorption of gases, with special reference to the evaluation of surface area and pore size distribution, Pure Appl. Chem. 87 (2015) 1051–1069.

[39] L. López Pérez, V. Zarubina, H.J. Heeres, I. Melián-Cabrera, Condensation-enhanced self-assembly as a route to high surface area α-aluminas, Chem. Mater. 25 (2013) 3971–3978.

[40] I. Melián-Cabrera, M. López Granados, J.L.G. Fierro, Bulk and surface structures of palladium-modified copper-zinc oxides ex hydroxycarbonate precursors, Chem.

[41] I. Melián-Cabrera, M. López Granados, J.L.G. Fierro, Pd-modified Cu–Zn catalysts for methanol synthesis from CO_2/H_2 mixtures: catalytic structures and performance, J. Catal. 210 (2002) 285–294.

[42] C.D. Wagner, L.E. Davis, M.V. Zeller, J.A. Taylor, R.H. Raymond, L.H. Gale, Empirical atomic sensitivity factors for quantitative analysis by electron spectroscopy for chemical analysis, Surf. Interface Anal. 3 (5) (1981) 211–225.

[43] W. Qi, W. Liu, B. Zhang, X. Gu, X. Guo, D.S. Su, Oxidative dehydrogenation on nanocarbon: identification and quantification of active sites by chemical titration, Angew. Chem. Int. Ed. 52 (2013) 14224–14228.

[44] G. Beamson, D. Briggs, High Resolution XPS of Organic Polymers - The Scienta ESCA300 Database, Wiley Interscience, New York, USA, 1992.

[45] G. Wen, J. Diao, S. Wu, W. Yang, R. Schlögl, D.S. Su, Acid properties of nanocarbons and their application in oxidative dehydrogenation, ACS Catal. 5 (2015) 3600–3608.

[46] K.E. Moore, D.D. Tune, B.S. Flavel, Double-walled carbon nanotube processing, Adv. Mater. 27 (2015) 3105–3137.

[47] F. Herold, J. Gläsel, B.J.M. Etzold, M. Rønning, Can temperature-programmed techniques provide the gold standard for carbon surface characterization? Chem. Mater. 34 (2022) 8490–8516.

[48] M. Sethurajan, E.D. van Hullebusch, D. Fontana, A. Akcil, H. Deveci, B. Batinic, J.P. Leal, T.A. Gasche, M. Ali Kucuker, K. Kuchta, I.F.F. Neto, H.M.V.M. Soares, A. Chmielarz, Recent advances on hydrometallurgical recovery of critical and precious elements from end of life electronic wastes - a review, Crit. Rev. Environ. Sci. Technol. 49 (3) (2019) 212–275.

[49] Y. Chen, L. Wei, B. Wang, S. Lim, D. Ciuparu, M. Zheng, J. Chen, C. Zoican, Y. Yang, G.L. Haller, G.L. Haller, L.D. Pfefferle, Low-defect, purified, narrowly (n, m)-dispersed single-walled carbon nanotubes grown from cobalt-incorporated MCM-41, ACS Nano. 1 (2007) 327–336.

[50] A. Jorio, M.A. Pimenta, A.G. Souza Filho, R. Saito, G. Dresselhaus, M.S. Dresselhaus, Characterizing carbon nanotube samples with resonance Raman scattering. New J. Phys. 5 (2003) 139.1–139.17.

[51] J.H. Lehman, M. Terrones, E. Mansfield, K.E. Hurst, V. Meunier, Evaluating the characteristics of multiwall carbon nanotubes, Carbon 49 (2011) 2581–2602.

[52] M. Thommes, Physical adsorption characterization of nanoporous materials, Chem. Ing. Tech. 82 (2010) 1059–1073.

[53] I. Melian-Cabrera, S. Espinosa, J.C. Groen, B. v/d Linden, F. Kapteijn, J.A. Moulijn. Utilizing full-exchange capacity of zeolites by alkaline leaching: Preparation of Fe-ZSM5 and application in N_2O decomposition, J. Catal. 238 (2006) 250–259.

[54] J. Laudenbach, D. Schmid, F. Herziger, F. Hennrich, M. Kappes, M. Muoth, M. Haluska, F. Hof, C. Backes, F. Hauke, A. Hirsch, J. Maultzsch, Diameter dependence of the defect-induced Raman modes in functionalized carbon nanotubes, Carbon 112 (2017) 1–7.

[55] M.T. Martínez, M.A. Callejas, A.M. Benito, M. Cochet, T. Seeger, A. Ansón, J. Schreiber, C. Gordon, C. Marhic, O. Chauvet, J.L.G. Fierro, W.K. Maser, Sensitivity of single wall carbon nanotubes to oxidative processing: structural modification, intercalation and functionalisation, Carbon 41 (2003) 2247–2256.

[56] I. Melián-Cabrera, V. Zarubina, Selectivity-induced conversion model explaining the coke-catalysed O_2-mediated styrene synthesis over wide-pore aluminas, Mol. Catal. 524 (2022) 112301.

[57] J.J. Mercadal, D. Osadchii, V. Zarubina, M.J. Valero-Romero, I. Melián-Cabrera, Organocatalyst reactivation with improved performance in O_2-mediated styrene synthesis, Mol. Catal. 529 (2022) 112525.

[58] A.E. Lisovskii, C. Aharoni, Carbonaceous deposits as catalysts for oxydehydrogenation of alkylbenzenes, Catal. Rev. Sci. Eng. 36 (1994) 25–74.

[59] M. Jerigová, M. Odziomek, N. López-Salas, "We Are Here!" Oxygen functional groups in carbons for electrochemical applications, ACS Omega 7 (2022) 11544–11554.

[60] W. Qi, W. Liu, X. Guo, R. Schlögl, D.S. Su, Oxidative dehydrogenation on nanocarbon: intrinsic catalytic activity and structure-function relationships, Angew. Chem. Int. Ed. 54 (2015) 13682–13685.

[61] X. Guo, W. Qi, W. Liu, P. Yan, F. Li, C. Liang, D.S. Su, Oxidative dehydrogenation on nanocarbon: revealing the catalytic mechanism using model catalysts, ACS Catal. 7 (2017) 1424–1427.